Virtual Acoustic Detector Arrays for All-Optical Ultrasound Sensing

Zesheng Zheng[a], Ruochong Zhang[b], Renzhe Bi[b], Malini Olivo[b], Kaicheng Liang[a,c,d,*]

[a]*Institute of Microelectronics, A*STAR, 2 Fusionopolis Way, Singapore 138634;*
[b]*A*STAR Skin Research Labs, A*STAR, 8A Biomedical Grove, Singapore 138648;*
[c]*Institute of Molecular and Cell Biology, A*STAR, 61 Biopolis Dr, Proteos, Singapore 138673;*
[d]*Lee Kong Chian School of Medicine, Nanyang Technological University, 59 Nanyang Dr, Singapore 636921.*
[*] *Corresponding author email: Liang_Kaicheng@imcb.a-star.edu.sg*

ABSTRACT

We introduce a compact, non-contact multimodal imaging platform that integrates ultrasound (US) imaging, inclusive of photoacoustic (PA) detection, with optical coherence tomography (OCT). This integration is achieved through a novel virtual acoustic detector array (VADA) technique for all-optical US sensing, utilizing the temporal and spatial resolving capabilities of swept-source optical interferometry. The technique extracts US signals from the phase time evolution of a swept-source OCT's spectral sweep. It enables the virtual construction of the VADA along both lateral and depth directions on the imaging target for non-contact detection of acoustic waves from surrounding US sources. The platform's high-speed scanning (MHz OCT A-scan rate) and ultra-sensitive phase detection (nm displacement sensitivity) allow for the customization of the spatial density of the VADA and the collection of wideband acoustic signals, which are essential for the reconstruction of US images. In our pilot study, we successfully demonstrated the feasibility of this technique. We used a conventional US transducer as an acoustic source. The acoustic field distribution within the imaging target and the morphology and position of the piezoelectric layer were successfully reconstructed, which is based on US waveforms obtained from the VADA.

Keywords: Photoacoustic (PA) imaging, ultrasound (US) reconstruction, optical coherence tomography (OCT), photoacoustic remote sensing (PARS), all-optical, noncontact, dual-modal imaging.

1. INTRODUCTION

The detection of ultrasound (US) propagation is crucial in many industrial and biomedical applications, serving diverse purposes from material characterization [1-3] and patient diagnosis [4, 5]. Traditional US detection methods typically necessitate direct contact with the biological sample or industrial component, presenting limitations in scenarios where noncontact is preferred or essential [6, 7]. Advancements in PA Microscopy (PAM) have been achieved, encompassing both interferometric [8] and non-interferometric [9] PA remote sensing (PARS) techniques. These developments provide critical non-invasive imaging capabilities essential for detailed cellular and tissue analysis. These methods are also beneficial for examining hazardous parts where contact might be impractical. However, existing noncontact methods often face challenges in either specifying the exact detection locations [10, 11] or in providing a sufficiently sampled US signal with MHz temporal resolution [12, 13].

This work introduces a system that employs Swept-Source Optical Coherence Tomography (SS-OCT) to detect US waves and create US images in a non-contact manner. With this system, the Virtual Acoustic Detector Array (VADA) is constructed to receive US raw data at high temporal resolution from specific sensing locations across both lateral and axial depths. The VADA allows for flexible locating of detector while preserving signal quality at the point of detection, adding versatility in aligning the US excitation source and the detection path. As a result, the VADA can achieve both precise spatial sensing localization and high temporal resolution, which is essential for various depth-resolved acoustic imaging applications. This contrasts with current PARS methods requiring co-focusing of excitation and probe beams and using maximum amplitude projection for pixel values, as seen in optical resolution-PAM implementation [11, 14, 15]. The development presented in this work expands the possible configurations and broadens the application spectrum in US sensing and imaging.

2. METHODS

1.1 Proposed system structure

The proposed detection system, as shown in Fig. 1, primarily utilizes: 1) SS-OCT, following a specialized protocol from 2) the acquisition & post-processing unit to acquire raw reflected optical signals embedded with US information for US images creation; 3) an US excitation source, where the generation of US can be achieved through various means such as the absorption of laser energy in techniques like PA and laser ultrasonics, as well as through piezoelectric transduction, mechanical loading, Lorentz force, air pulses, heartbeats, among others; 4) The US detection arm, which can have various configurations to align with different US applications, e.g., PA microscopy, PA tomography, and US imaging and ranging.

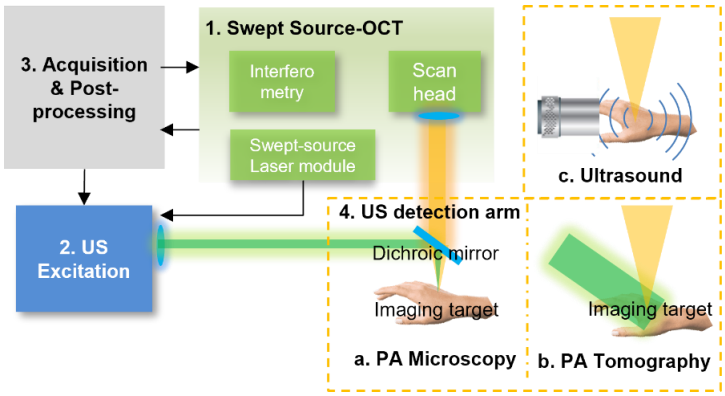

Fig. 1. Proposed system structure.

1.2 SS-OCT A-scan acquisition.

The SS-OCT subsystem operates on the principle of interferometry, where the phase variation in the OCT fringes can reveal US-induced vibrational displacement at the nanometer scale within the sample [16, 17]. The schematics in Fig. 2 depict the raw data acquisition process in the detection arm: The red circle indicates the US source, the blue dotted circles show the US propagation from the source to the surrounding medium, and the OCT detection beam (in orange) points down to the target, defining the current US sensing region.

The sweep period of the high-speed SS-OCT, specifically the OCT A-scan time (< 1 us), can be shorter than the time required for the US to propagate from the source to the sensing region (up to tens of us). In such case, within one complete acquisition cycle (from T_0 to T_N, , as shown in Fig. 2), multiple successive OCT A-scans are required at a stationary beam location $x=x_0$ to cover the entire US propagation: the acquisition timing T0 for OCT A-scan 0 is synchronized with the moment of US wave emission, the subfigures indicate the timing of the subsequent OCT A-scans (1 to N), and the acquisition cycle continues until the US has propagated through the sensing region $x=x_0$, where the peak arrives between time T_{N-1} and T_N. In this cycle, a total of N OCT A-scans is performed to capture the complete US waveform. The cycle can be performed at different OCT beam locations to extend the lateral field of view, i.e., the aperture of the VADA.

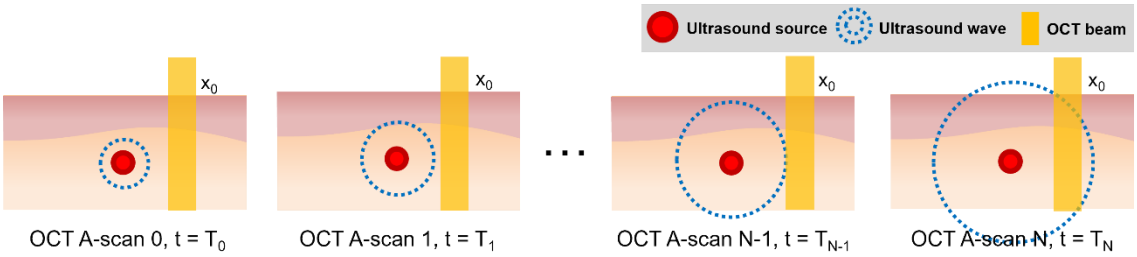

Fig. 2. One OCT raw data acquisition cycle in the detection arm.

1.3 US A-scan extraction at VADA locations

VADA can be constructed from the raw OCT data with US A-scans extracted at each detector location. Among different type of OCT systems (e.g., time-domain OCT, spectral-domain OCT, and SS-OCT), SS-OCT is exclusively selected since it can achieve both:

a) Depth-resolved VADA detector location: Since OCT is capable of producing depth-resolved images of the target structure (the greyscale background in Fig. 3a)), each pixel (represented by squares)—or a cluster of surrounding pixels along the axial (depth) direction can function as a well-defined positional element within

a VADA. The highlighted pixel at (x_0, z_0) in Fig. 3a&e serves as an example. Fig. 3b-d illustrate the pixel's respective time-domain, frequency-domain representations, and the time-domain instantaneous phase. In the time domain (Fig. 3a), the data can be formulated as follows:

$$x(k) = A\cos(zk); \tag{1.1}$$

Where A is the amplitude constant, k is the wavenumber of the swept source laser, and z represents the frequency of the fringes. In other words, z indicates the depth of the pixel, as illustrated in Fig. 3a and c.

The US data is denoted as $\Phi_n(t)$, which is a time series. Given that the output wavenumber k of the SS-OCT is correlated with time, the US data can be remapped to:

$$\Phi_n(t) \rightarrow \Phi_n(k); \tag{1.2}$$

As the US wave arrives at the detector pixel (as shown in Fig. 3e), it contribute to the original fringe (1.1) as a phase noise term (depicted in blue in Fig. 3f). Consequently, the fringe formula becomes:

$$x(k) = A\cos[zk + \Phi_n(k)]; \tag{1.3}$$

Therefore, power of the fringe signal is dispersed to adjacent frequencies, leading to the creation of noise sidebands [18, 19]. Fig. 3g plots its frequency spectrum, demonstrating that the US spectrum $[z_{n,\min}, z_{n,\max}]$ is shifted and centered at the OCT fringe frequency, corresponding to pixel depth z_0. It demonstrates that by applying a band-pass filter to the acquired raw OCT data at z_0, not only the individual VADA detector can be located, but the received US data is also preserved.

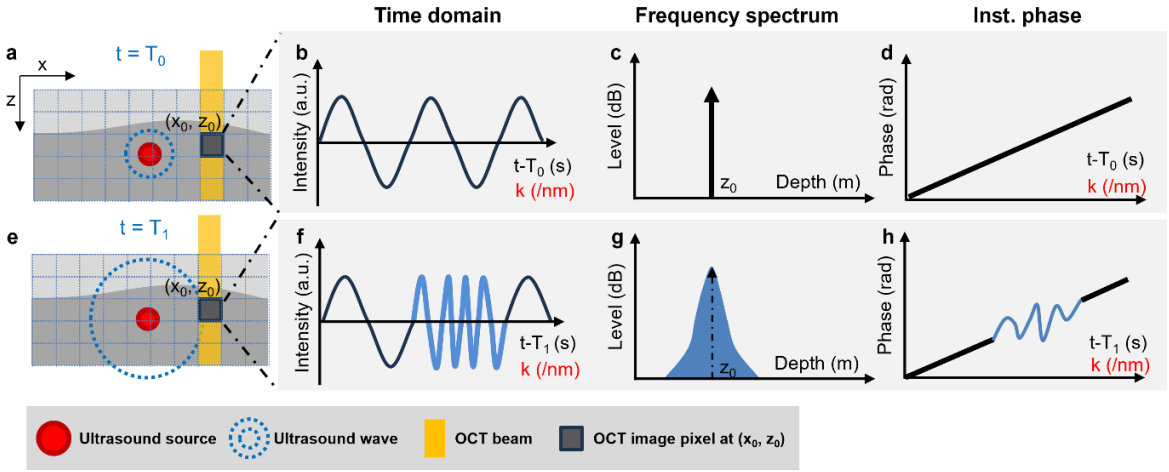

Fig. 3 US data as phase modulation term in the oct pixels (VADA elements). a-d the schematic and OCT data without the US data detected. e-h. the schematic and OCT data with the US data detected. Illustration is exaggerated and not to scale.

b) High temporal resolution US data: The instantaneous phase of the fringes at each detector location, both without and with the detected US, can be computed via time frequency analysis. The former (illustrated in Fig. 3d) serves as the reference baseline, while the latter (shown in Fig. 3h) can be subtracted from this baseline to obtain the US data $\Phi_n(k)$. This data can then be remapped back to time domain:

$$\Phi_n(k) \rightarrow \Phi_n(t); \tag{1.4}$$

The acquisition rate of the time series depends on the acquisition card, ranging from hundredths of MHz to GHz. Generally, this rate is more than sufficient to capture US data up to tens of MHz. However, due to the uncertainty principle of time-frequency analysis, a careful trade-off must be made between the size of the VADA detector (spectrum width) and the temporal resolution.

3. RESULTS

As illustrated in Fig. 4, a scotch tape sample is placed under the OCT objective in this experiment. A conventional piezoelectric transducer (with a center frequency of 10 MHz) serves as the US source. Its focus spot is approximately positioned at the side wall of the tape sample. The OCT beam sweeps laterally across the tape top surface, forming a 3D VADA comprised of 101 x 20 x 20 points. These points are distributed within a volume

measuring 9 mm (x axis) x 1.7 mm (y axis) x 1.3 mm (z axis), where the first and second dimensions lie along the lateral plane, and the third dimension is constructed along the depth direction.

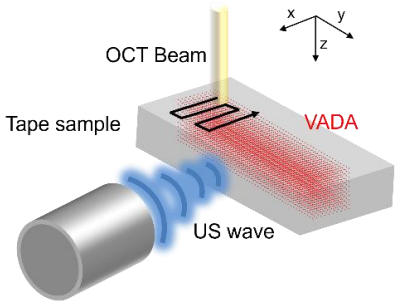

Fig. 4 Experiment setup and VADA.

Fig. 5a shows a sequence of OCT images overlaid with the corresponding maximum amplitude projection (MAP) of the acquired US data at each VADA location, specifically the acoustic field distribution inside the tape. Utilizing the raw US data collected from each VADA detector location (example given in Fig. 5b), various acoustic reconstruction algorithms can be applied to reconstruct the US source. These algorithms may include time reversal [20], time-domain [21, 22], model-based [23], and frequency domain [24] methods. Fig. 5c displays the morphology and position of the piezoelectric layer of the US transducer reconstructed with time reversal (k-wave toolbox [25]). It should be noted that the signals extracted from outside the tape region, which exhibit strong MAP, are system random phase noise across the entire sequence. They possess different temporal and frequency components compared to the normal US data and thus will be eliminated during the reconstruction process.

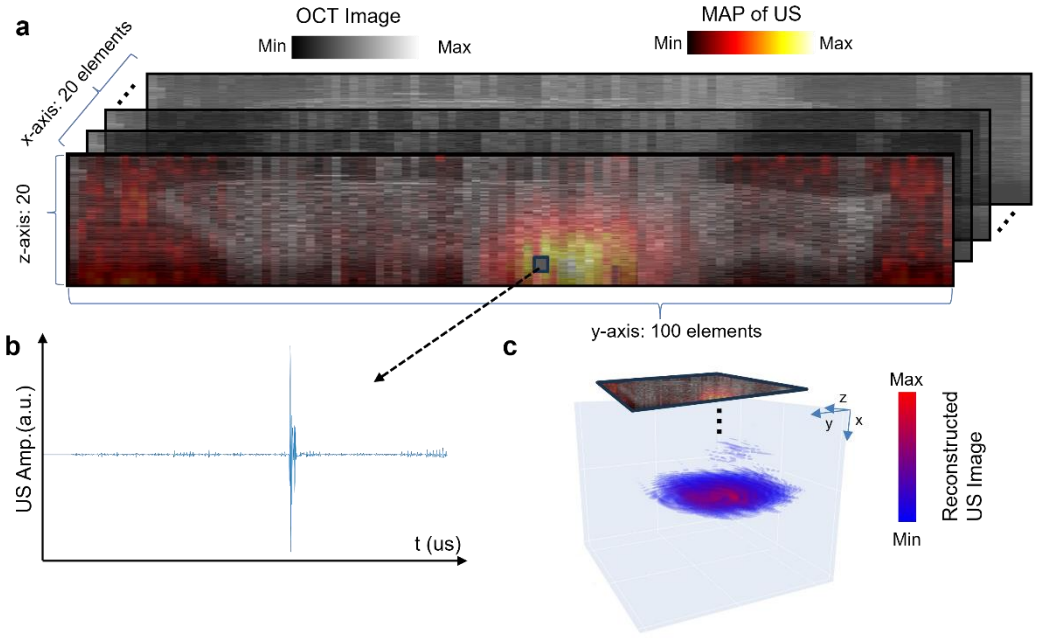

Fig. 5 The US data from the VADA and the reconstructed image. a. a sequence of OCT image overlaid with the MAP of the US data at each VADA element; c. example raw US data at one VADA element; c. the reconstructed US source.

4. CONCLUSION

The study introduces the VADA for noncontact sensing and imaging of US and PA, a technique crucial in various industrial and biomedical fields. We have described the system structure and formulated its underlying principles. Our experiment in obtaining acoustic field distribution within the tape and reconstructing the US source has successfully illustrated the feasibility of this method. The most notable achievement of VADA is its ability to spatially distribute the detector array along the depth dimension inside the OCT target to characterize the acoustic field distribution and acquiring US waveform. This approach not only enhances the quality of reconstructed US imaging with a high-density array but also enables new configurations previously unexplored and physically infeasible, thereby broadening the potential applications.

ACLKNOWLEDGEMENT

This work was supported by fundings: National Research Foundation Singapore (NRFF13-2021-0002); Manufacturing, Trade and Connectivity (MTC) Individual Research grant (M22K2c0089); Agency for Science, Technology and Research.

REFERENCES

[1] S. K. Dwivedi, M. Vishwakarma, and P. A. Soni, "Advances and Researches on Non Destructive Testing: A Review," Materials Today: Proceedings, 5(2), 3690-3698 (2018).
[2] M. Tanter, and M. Fink, "Ultrafast imaging in biomedical ultrasound," IEEE Transactions on Ultrasonics, Ferroelectrics, and Frequency Control, 61(1), 102-119 (2014).
[3] J. L. Diaz-Gomez, P. H. Mayo, and S. J. Koenig, "Point-of-Care Ultrasonography," N Engl J Med, 385(17), 1593-1602 (2021).
[4] M. Xu, and L. V. Wang, "Photoacoustic imaging in biomedicine," Review of Scientific Instruments, 77(4), (2006).
[5] P. Beard, "Biomedical photoacoustic imaging," Interface Focus, 1(4), 602-31 (2011).
[6] Z. Hosseinaee, M. Le, K. Bell *et al.*, "Towards non-contact photoacoustic imaging [review]," Photoacoustics, 20, 100207 (2020).
[7] G. Rousseau, B. Gauthier, A. Blouin *et al.*, "Non-contact biomedical photoacoustic and ultrasound imaging," J Biomed Opt, 17(6), 061217 (2012).
[8] F. Yang, Z. Chen, and D. Xing, "All-optical noncontact phase-domain photoacoustic elastography," Opt Lett, 46(19), 5063-5066 (2021).
[9] P. Hajireza, W. Shi, K. Bell *et al.*, "Non-interferometric photoacoustic remote sensing microscopy," Light Sci Appl, 6(6), e16278 (2017).
[10] S. Song, Z. Huang, and R. K. Wang, "Tracking mechanical wave propagation within tissue using phase-sensitive optical coherence tomography: motion artifact and its compensation," J Biomed Opt, 18(12), 121505 (2013).
[11] M. Martell, N. J. Haven, and R. Zemp, "Fiber-based photoacoustic remote sensing microscopy and spectral-domain optical coherence tomography with a dual-function 1050-nm interrogation source," J Biomed Opt, 26(6), (2021).
[12] Z. Ma, N. Ding, Z. Li *et al.*, "Spectral interference contrast based non-contact photoacoustic microscopy realized by SDOCT," Opt Lett, 47(11), 2895-2898 (2022).
[13] R. Li, Z. Du, X. Qian *et al.*, "High resolution optical coherence elastography of retina under prosthetic electrode," Quant Imaging Med Surg, 11(3), 918-927 (2021).
[14] M. T. Martell, N. J. M. Haven, and R. J. Zemp, "Multimodal imaging with spectral-domain optical coherence tomography and photoacoustic remote sensing microscopy," Opt Lett, 45(17), 4859-4862 (2020).
[15] Y. Yuan, X. Wen, B. Yuan *et al.*, "Photoacoustic remote sensing elastography," Opt Lett, 48(9), 2321-2324 (2023).
[16] D. C. Adler, R. Huber, and J. G. Fujimoto, "Phase-sensitive optical coherence tomography at up to 370,000 lines per second using buffered Fourier domain mode-locked lasers," Opt Lett, 32(6), 626-8 (2007).
[17] Y. Li, S. Moon, J. J. Chen *et al.*, "Ultrahigh-sensitive optical coherence elastography," Light Sci Appl, 9, 58 (2020).
[18] W. P. Robins, [Phase Noise in Signal Sources], (1984).
[19] A. Hajimiri, and T. H. Lee, "A general theory of phase noise in electrical oscillators," IEEE Journal of Solid-State Circuits, 33(2), 179-194 (1998).
[20] M. Fink, "Time reversal of ultrasonic fields. I. Basic principles," IEEE Trans Ultrason Ferroelectr Freq Control, 39(5), 555-66 (1992).
[21] G. Matrone, A. S. Savoia, G. Caliano *et al.*, "The delay multiply and sum beamforming algorithm in ultrasound B-mode medical imaging," IEEE Trans Med Imaging, 34(4), 940-9 (2015).
[22] G. Paltauf, R. Nuster, and P. Burgholzer, "Weight factors for limited angle photoacoustic tomography," Phys Med Biol, 54(11), 3303-14 (2009).
[23] X. L. Dean-Ben, A. Buehler, V. Ntziachristos *et al.*, "Accurate model-based reconstruction algorithm for three-dimensional optoacoustic tomography," IEEE Trans Med Imaging, 31(10), 1922-8 (2012).
[24] Y. Xu, D. Feng, and L. V. Wang, "Exact frequency-domain reconstruction for thermoacoustic tomography--I: Planar geometry," IEEE Trans Med Imaging, 21(7), 823-8 (2002).
[25] B. E. Treeby, and B. T. Cox, "k-Wave: MATLAB toolbox for the simulation and reconstruction of photoacoustic wave fields," J Biomed Opt, 15(2), 021314 (2010).